ELSEVIER

Journal of Nuclear Materials 280 (2000) 318–330

journal of nuclear materials

www.elsevier.nl/locate/jnucmat

In situ XRD analysis of the oxide layers formed by oxidation at 743 K on Zircaloy 4 and Zr–1NbO

N. Pétigny [a], P. Barberis [b,*], C. Lemaignan [c], Ch. Valot [a], M. Lallemant [b,†]

[a] *Laboratoire de Recherche sur la Réactivité des Solides, Université de Bourgogne, BP 400, 9 Avenue Alain Savary, 21011 Dijon cedex, France*

[b] *Cézus, Centre de Recherche Ugine, 73403 Ugine cedex, France*

[c] *CEA, Grenoble, 17 rue des Martyrs, 38054 Grenoble cedex 9, France*

Received 27 October 1999; accepted 4 April 2000

Abstract

Two alloys, having different oxidation behaviour (Zy4 and Zr–1NbO), have been investigated during oxidation at high temperature (743 K) and low oxygen pressure (10 kPa) by in situ X-ray diffraction (XRD). Tetragonal phase content and 'pseudo-stresses' on the monoclinic phase have been measured as a function of the oxide layer thickness. The tetragonal phase contents are similar for both alloys and decreased with the oxide layer thickness. Pseudo-stresses were much more compressive on Zr–1NbO alloy, with limited changes at the corrosion kinetics transition. On cooling, the tetragonal fractions do not change, while 'pseudo-stresses' decreased in different ways for the two alloys. With respect to stress analysis, no correlation was found between 'pseudo-stresses' and tetragonal phase content. In addition, due to the thermoelastic properties of the highly anisotropic phases of the zirconia, large internal thermal stresses are expected to develop during any temperature changes. The orders of magnitude of them are similar to the stresses induced by swelling during oxidation from Zr to ZrO_2. © 2000 Elsevier Science B.V. All rights reserved.

1. Introduction

The increase in burn-up of nuclear fuels planned by the nuclear power plants in the recent years led to the development of zirconium alloys more resistant to corrosion than the Zy4, like Zr–Nb alloys. It is observed that the Zr–Nb alloys exhibit a different corrosion mechanism, the initial kinetic being parabolic, rather than cubic for Zy4, and show a much weaker corrosion kinetics transition. A better understanding of the origins of these differences requires an in-depth analysis of the relations between the corrosion kinetics and the microstructural or physical features of the oxide layer, like tetragonal phase content, stresses and textures. Indeed, despite numerous studies undertaken in different countries [1–7], several steps of the process still remain unclear. Among others, the following questions remain open:

1. Why is the metastable tetragonal phase observed in the oxide layer?
2. How is the expansion from Zr to ZrO_2 (Pilling–Bedworth ratio of 1.56) shared in the three directions of the oxide layer, inducing strains and stresses?
3. How is the kinetic transition linked to stress relaxation or to crack formation?

An important additional question arises from the fact that measurements are generally performed at room temperature, after cooling from the high temperature oxidations. Any change in the phase content or thermal strains during these temperature decreases, would affect the results, and the measurements performed at room temperature cannot be used without corrections to explain a specific mechanism expected to be active during the oxidation at high temperature.

---

[*] Corresponding author. Tel.: +33-4 79 89 30 68; fax: +33-4 79 89 35 00.

E-mail address: barberis.crcezus@uginesavoie.usinor.com (P. Barberis).

[†] Deceased.

PII: S0022-3115(00)00051-9

The aim of this paper is then to analyse, by X-ray diffraction (XRD) in situ and after cooling, the phase contents and the stresses in the oxide layers developed on Zy4 and on Zr–1NbO during high temperature oxidation.

2. Experimental procedure

2.1. Materials and oxidation conditions

The alloys chosen for this study (zircaloy 4 and Zr–1NbO) were provided as 1 mm thick recrystallized sheets processed at laboratory scale by CEZUS. The compositions of the alloys are given in Table 1. Out of the plates, rectangular samples (8 × 10 mm) were machined, mechanically polished and chemically etched in a nitro–fluoric mixture ($H_2O/HNO_3/HF$:50/43/7).

The oxidation tests have been performed under 10^4 Pa of oxygen at 743 K, conditions chosen for a convenient balance between reasonable experiment duration and significant oxide thickness. In order to avoid any drift in measurements during the experiments, the oxidation time did not exceed 15 days. This allowed the oxidation reaction to be slow enough to consider the sample unchanged during each X-ray data acquisition step. In addition, the kinetic curves were obtained during oxidation within a thermo-balance, allowing a continuous recording of the mass changes.

2.2. XRD measurements and data processing

In order to perform the measurements at elevated temperature, an X-ray diffractometer was equipped with a furnace surrounded by a chamber for environment control, having Be windows for the X-ray beams. XRD spectra have been obtained in situ and after cooling, using a θ/θ configuration and diffracted intensities recorded with a 10° linear counter. Cr K_α radiation measurement conditions are given in more detail in Table 2.

With the same device, phase fraction analysis and residual stress measurements can be made, without removing the sample from holding stage. Cr K_α radiation was used for ‘pseudo-stress’ determination, while Cu K_α radiation was chosen to measure the tetragonal phase fraction. The system absolute accuracy was 0.1°, as controlled with iron powder. Both the $K_{\alpha1}$ and $K_{\alpha2}$ wavelengths contribute to the intensities, but have been separated using the PROFILE/DIFFRACT-AT software, to obtain the intensities and the positions of the diffraction peaks.

Table 2
XRD conditions for stress analysis in m_{ZrO_2}

Tension/current (Cr K_α)	30 kV/16 mA
Beam diameter	2 mm
Diffraction plane	$(\bar{1}\,0\,4)_{m_{ZrO_2}}$
2θ Bragg angle	120.03°
1/2 S_2 ($h\,k\,l$) isotropic	10.04×10^{-6} MPa^{-1}
Acquisition time per ψ angle	250 s
ψ angle range	−41° to 41° with 3° step

In order to get the tetragonal phase fractions, the spectrometer was set in Bragg's incidence on (1 1 1) tetragonal peak ($2\theta = 30.1°$) so that planes parallel to the oxide/metal interface were analysed. A typical acquisition time was 600 s. The stress determinations were performed on the monoclinic phase only, under the conditions described in Table 2.

2.2.1. Tetragonal volume fraction determinations

Several authors [4,8–10] have already given expressions for isotropic zirconia powder mixtures. The proportions of each phase can be expressed by

$$X_m = \frac{I_m(1\,1\,1) + I_m(\bar{1}\,1\,1)}{I_m(1\,1\,1) + I_m(\bar{1}\,1\,1) + I_t(1\,1\,1)} \quad \text{and} \quad X_t = \frac{I_t(1\,1\,1)}{I_m(1\,1\,1) + I_m(\bar{1}\,1\,1) + I_t(1\,1\,1)}, \tag{1}$$

where X_i is the bulk volume fraction of the phase i, monoclinic or tetragonal, $I_i(h\,k\,l) = I'_i(h\,k\,l)/R_i(h\,k\,l)$ the reflected intensity of the phase i for the plane ($h\,k\,l$), $I_i'(h\,k\,l)$ and $R_i(h\,k\,l)$ are the measured peak intensity and the corresponding structure factor, respectively.

However, in the case of the oxidation of Zr alloys, the oxide layer is highly textured, and the measured intensities should be corrected for this effect. As proposed by Valot [10], $I'_i(h\,k\,l)$ should be replaced by $I'_i(h\,k\,l)/n_i(h\,k\,l)$, where the $n_i(h\,k\,l)$ are the reflecting lattice plane number fractions deduced from the pole figure and the orientation of the sample (ψ, φ) by the following equation:

Table 1
Composition of the alloys studied

Alloy	%Sn	%Nb	O_2 (ppm)	Fe (ppm)	Cr (ppm)
Zr–1%NbO	–	0.96	1140	147	50
Zy 4	1.34	–	1236	2220	1131

$$C(h\,k\,l) = \frac{\int_0^{\pi/2}\int_0^{2\pi} I_{\psi\phi}\sin\psi\,\mathrm{d}\psi\,\mathrm{d}\phi}{\int_0^{\pi/2}\int_0^{2\pi}\sin\psi\,\mathrm{d}\psi\,\mathrm{d}\phi},$$
$$n_{\psi\phi}(h\,k\,l) = \frac{I_{\psi\phi}}{C(h\,k\,l)}. \tag{2}$$

The texture of the monoclinic phase has been measured after cooling, but it can reasonably be assumed that it does not evolve significantly in temperature. Indeed major changes in texture of the phases would require a complete recrystallization of the oxide layer during cooling. This would not be consistent with the observations performed by TEM on similar oxide layers [11,12].

2.2.2. Phase gradients analysis

The diffracted intensities are average values, which depend on several factors such as the incidence angle, θ_i as indicated by Eq. (3):

$$I(\theta_\mathrm{i}) \propto \frac{S_0|F(h\,k\,l)|^2}{\sin\theta_\mathrm{i}}\cdot \mathrm{LP}\cdot n(h\,k\,l)\cdot p\int_0^h q(z)\mathrm{e}^{-\mu' z}\,\mathrm{d}z, \tag{3}$$

where S_0 is the irradiated surface; $F(h\,k\,l)$ represents the structure factor; LP the Lorentz polarization factor (it was computed for the (1 1 1) peak of the Ge single crystal used as monochromator); θ_i the incident angle; $n_\mathrm{i}(h\,k\,l)$ the texture factor; p the multiplicity factor; $q(z)$ the local quantity of the analyzed phase, at depth z (it is equivalent to $t(z)$ or $m(z)$, respectively, for the tetragonal and monoclinic phases);

$$\mu' = \mu\left(\frac{1}{\sin\theta_\mathrm{i}} + \frac{1}{\sin(2\cdot\theta_{h\,k\,l} - \theta_\mathrm{i})}\right)$$

a correction factor for the X-ray absorption by the material and h is the oxide layer thickness.

Since the quantities $t(z)$ and $m(z)$, respectively, represent local intensities of tetragonal and monoclinic zirconia, the sum of these two intensities must be constant whatever be the localization in the volume element analysed in the oxide layer. Several expressions (linear, polynomial and exponential) have been tested as possible depth dependency of the phase contents, and the best results were obtained with the exponential profiles. Thus, the data were adjusted to the following expressions:

$$t(z) = A\exp(Bz) \quad \text{and} \quad m(z) = C - A\exp(Bz), \tag{4}$$

where A, B and C are the fitting constants.

Using the relations (3) and (4) the analytical equations that have to be solved become

$$I((1\,1\,1)q,\theta_\mathrm{i}) = \frac{4.7\times10^3\cdot n(h\,k\,l)(\theta_\mathrm{i})}{\sin\theta_\mathrm{i}} \times\left\{\frac{A}{\mu'_q - B}(1-\mathrm{e}^{-\mu'_q h})\right\}, \tag{5}$$

$$I((\bar{1}\,1\,1)m,\theta_\mathrm{i}) = \frac{8.7\times10^3\cdot n(h\,k\,l)(\theta_\mathrm{i})}{\sin\theta_\mathrm{i}} \times\left\{\frac{C}{\mu'_m}(1-\mathrm{e}^{-\mu'_m h}) - \frac{A}{\mu'_m - B}(1-\mathrm{e}^{-(\mu'_m - B)h})\right\}. \tag{6}$$

The minimization of the normalized sum of errors

$$\frac{(I(h\,k\,l)_\mathrm{experimental} - I(h\,k\,l)_\mathrm{calculated})^2}{I(h\,k\,l)_\mathrm{experimental}}$$

gives access to the constants A, B and C, and then to the tetragonal content profile in the oxide layer.

2.2.3. 'Pseudo-stress' determination

2.2.3.1. Theoretical background. The elastic stress determination by XRD in crystalline material uses the lattice parameters as local strain gauges. 'Pseudo-stresses' have been determined on the $(\bar{1}\,0\,4)_\mathrm{m}$ planes of the monoclinic zirconia, as usually done in earlier studies on this subject [13,15]. As discussed later, this phase may not be in the same stress state as the tetragonal phase and what is measured has to be distinguished from the average stress level in the zirconia. Microstrains are described as in the relation (7)

$$\varepsilon = \left(\frac{d - d_0}{d_0}\right)_{h\,k\,l} = \left(\frac{\Delta d}{d_0}\right)_{h\,k\,l}, \tag{7}$$

where d_0 is the stress free interatomic distance of the $(h\,k\,l)$ reflecting plane.

By diffraction, the strains of the lattice are measured and then the elastic stresses are determined by the continuous mechanics analysis. In standard procedures, the material is considered to be homogeneous and isotropic. Lattice strains are assumed to be homogeneous in the analysed diffracting volume [16].

By using the so-called $\langle\sin^2\psi\rangle$ method, and because σ_{33} vanishes at the surface, the diffraction peak shift can be described as follows:

$$2\theta_{\phi\psi} = 2\theta_0 - \left(\frac{1}{2}S_2\right)\frac{360}{\pi}\tan\theta_0\left[\sigma_{11}^{\phi}\sin^2\psi + \sigma_{13}^{\phi}\ \sin(2\psi)\right] - (S_1)\frac{360}{\pi}\tan\theta_0\left[\sigma_{11}^{\phi} + \sigma_{22}^{\phi}\right], \tag{8}$$

where $2\theta_0$ is the stress free Bragg peak position, $1/2\ S_2$ and S_1 represent the elastic constants defined for an isotropic material by

$$\frac{1}{2}S_2 = \frac{1+v}{E} \quad \text{and} \quad S_1 = \frac{-v}{E}, \tag{9}$$

where ψ is the angle between the normal of the sample surface and one of the $(h\,k\,l)$ lattice plane, σ_{ij}^{ϕ} is the average stress intensity in the ϕ direction of the space (ϕ: in plane rotation of the sample).

For isotropic materials, the standard $2\theta_{\phi\psi} = f(\sin^2\psi)$ representation leads to an ellipse in the case where the primary stress axes are not parallel to the XRD equipment main axes. It reduces as a straight line for biaxial state ($\sigma_{11}^{\phi} = \sigma_{22}^{\phi}$ *et* $\sigma_{13}^{\phi} = 0$). The isotropic surface stress, σ_{11}, is deduced from the slope, p, providing that the average elastic constants are known.

$$p = -\left(\frac{1}{2}S_2\right)\frac{360}{\pi}\tan\theta_0\,\sigma_{11}^{\phi}. \tag{10}$$

In the case of crystal anisotropy, the elastic strains are linear function of the stresses through the stiffness tensor and are expressed by the relation

$$\varepsilon_{kl} = S_{ijkl}\sigma_{kl}, \tag{11}$$

where ε_{kl} are the components of the elastic strain tensor and S_{ijkl} are the compliance coefficients.

The growth of zirconia films on zirconium alloys leads usually to a fibre texture, which was observed to remain constant with the oxide thickness [17–19]. In that case, an orthotropic elastic model would be a more appropriate description [17] and the precise knowledge of the S_{ijkl} is necessary for stress determination from strain measurements. The existing models [20,21] have been developed for the cubic or hexagonal structures but they are not appropriate for monoclinic crystals. Moreover, no data exist for the elastic constants at high temperature. Furthermore, stress gradients could be expected and are not taken into account in the equations presented. All these considerations show that what is determined is not homogeneous bulk stresses but rather average 'pseudo-stresses', whose absolute values are questionable, but whose evolution can be considered, though cautiously.

When cooling a sample, thermal stresses add to the stresses that develop during oxidation. Though their computation is straightforward for a series of isotropic single-phase layers, the case of zirconium oxide films are much more difficult due to an oxide layer made of a crystallographically, elastically and thermoelastically anisotropic, textured, two phase material. A description of the parameters involved will be given in Section 4.

2.2.3.2. Experimental conditions and data processing. Performing XRD measurements during zirconium alloy oxidation requires an experimental setup where some constrains induced by the oxidation environment lead to non-ideal XRD conditions. Indeed, measurements were made at the rather low angle of 120° (2θ) for the $(\bar{1}\,0\,4)_{\mathrm{m}}$ peak to have a high enough diffracted intensity. In addition, this peak is close to two peaks of the Zr matrix: $(2\,0\,1)_{\mathrm{Zr}}$ and $(0\,0\,4)_{\mathrm{Zr}}$ and is rather broad, due to the very fine grain size [3,12]. Therefore, a careful procedure is required for peak fitting and extraction. These three overlapping components were extracted using the following manual procedure.

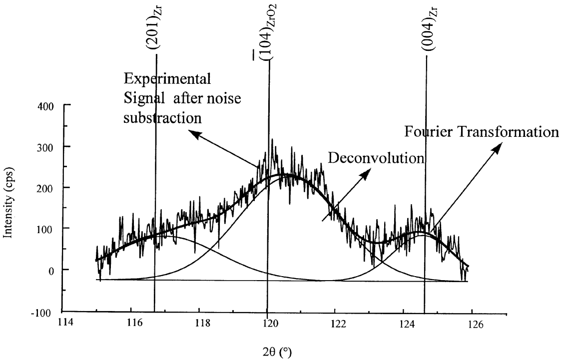

Fig. 1. Treatment for the pseudo-stress determination.

Data processing was performed with the ORIGIN software using the three following steps: (1) On each signal, the background noise is subtracted by linear interpolation from its value outside the peaks. (2) In order to improve signal-to-noise ratio, a Fourier Transformation Filter procedure is performed. (3) As clearly observed, three Gaussian peaks are assumed to be present for profile fitting, with a free position of each of them (Fig. 1). Each spectrum has been processed individually. Error bars displayed on the curves are taking into account all the experimental errors and uncertainties in the fitting procedures. Then, the $(\bar{1}\,0\,4)_{\mathrm{m}}$ peak position is obtained and the corresponding $2\theta_{\phi\psi} = f(\sin^2\psi)$ plots are drawn for both temperatures (Fig. 2). The 2θ vs ψ plots appear to be linear in both cases but the slope is more than twice as high at 743 K than at room temperature. As the stresses are directly linked to the slopes of these lines, the aim of the analysis is to explain such a significant difference between the measurements made at temperature and after cooling.

3. Results

3.1. Oxidation kinetic behaviour

The oxidation rates measured on the thermo-balance are plotted in Fig. 3. The Zr–1NbO oxidation rate in the environment tested is higher than one of the recrystallized Zy4. The kinetic 'transition', corresponding to corrosion acceleration, is more clearly pronounced for Zy4 than for Zr–1NbO. The difference is enhanced when plotting the thickness as a function of the inverse of the corrosion rate (Fig. 4). The Zr–1NbO oxidation shows a weak transition between the first parabolic rate and the

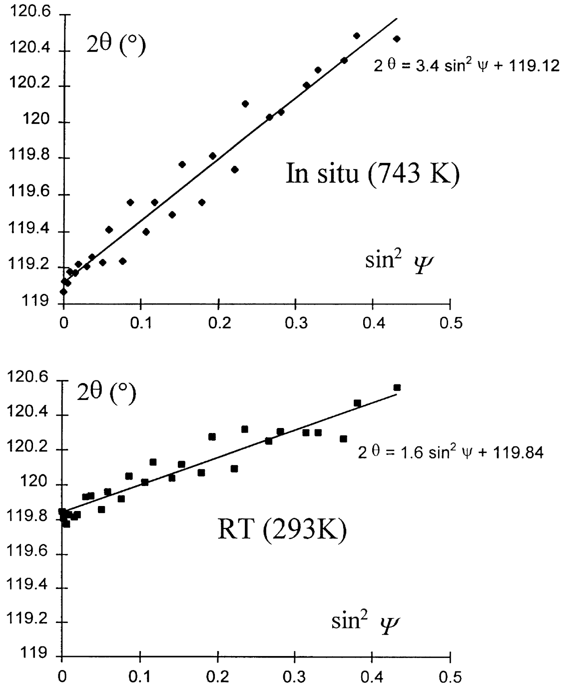

Fig. 2. $2\theta_{\phi\psi} = f(\sin^2\psi)$ for Zr–1NbO alloy measured in situ and after cooling at room temperature.

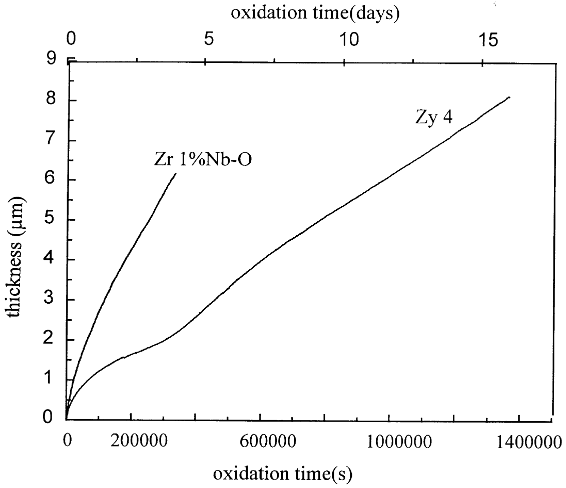

Fig. 3. Zr–1NbO and recrystallized Zy4 oxidation rate at 743 K under 10^4 Pa of oxygen.

second one observed at a thickness near 2.2 µm; at 5.1 µm, the oxidation rate becomes gradually linear. For the Zy4 oxidation, a sharp transition occurs at 2.1 µm and is more pronounced than the Zr–1NbO one. In order to understand the origin of this transition, these results will be compared later with the tetragonal phase content and stress evolutions.

3.2. Monoclinic and tetragonal phases

3.2.1. Texture of the monoclinic zirconia

Pole figures (PFs) have been recorded after cooling on samples with different thickness for the three peaks $(\bar{1}\,1\,1)_m$, $(1\,1\,1)_m$ and $(\bar{2}\,0\,2)_m$ of the monoclinic zirconia. No significant evolution of the texture appears when the

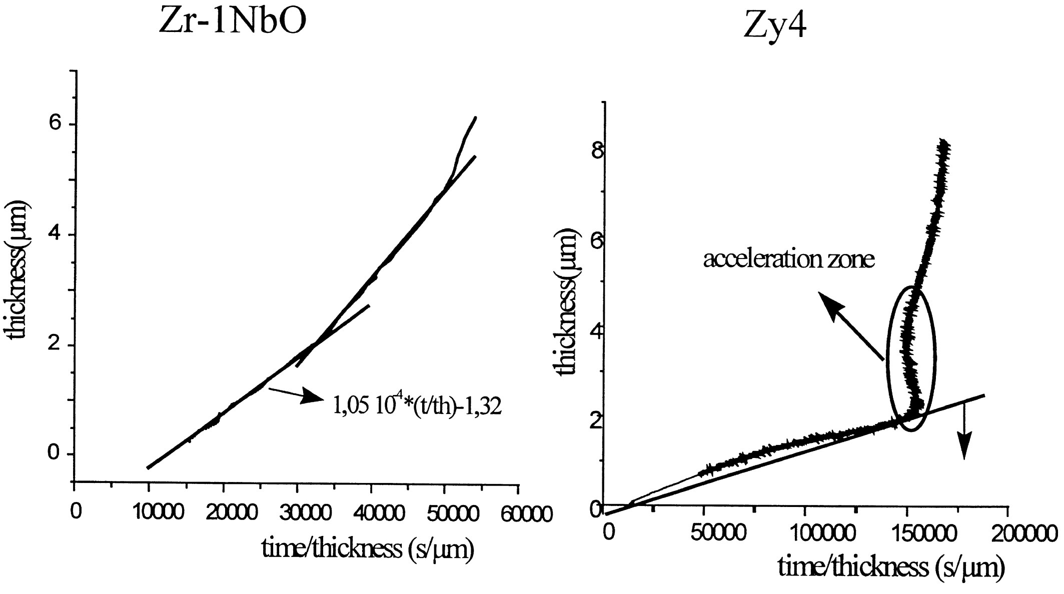

Fig. 4. Zr–1NbO and recrystallized Zy4 oxidation rate at 743 K under 10^4 Pa of oxygen ($e = f$(time/thickness) description).

oxide layer grows (Fig. 5) whatever the alloy composition. The PFs can be described as a free rotation for a 40° inclination and significant reinforcement between 35° and 40°. This analysis implies that the $(\bar{1}\,0\,k)_m$ planes are mostly parallel to the sample surface. Thus, the $(\bar{1}\,0\,4)_m$ and $(\bar{1}\,0\,3)_m$ planes are parallel to the surface of the sample (with no specific orientation to the rolling direction), and to a lesser extent the $(\bar{1}\,0\,2)_m$ and $(\bar{1}\,0\,1)_m$ planes also, slightly more oriented with respect to the rolling direction. This last preferential orientation could explain the reinforcement between 35° and 50° observed in the PFs (Fig. 5). The texture of the tetragonal phase was not attainable due to the low XRD intensity of the peaks specific to this phase.

Average values of the reflecting lattice plane numbers (corresponding to the Bragg angles) are given in Table 3. For each alloy, no evolution is observed for the oxide with respect to oxide layer thickness. The numbers are similar for the monoclinic peaks, but they vary significantly for the tetragonal phase from Zy4 to Zr–1%NbO. Due to the gradient in tetragonal phase fraction, these parameters are changing as the incident angle θ_i is

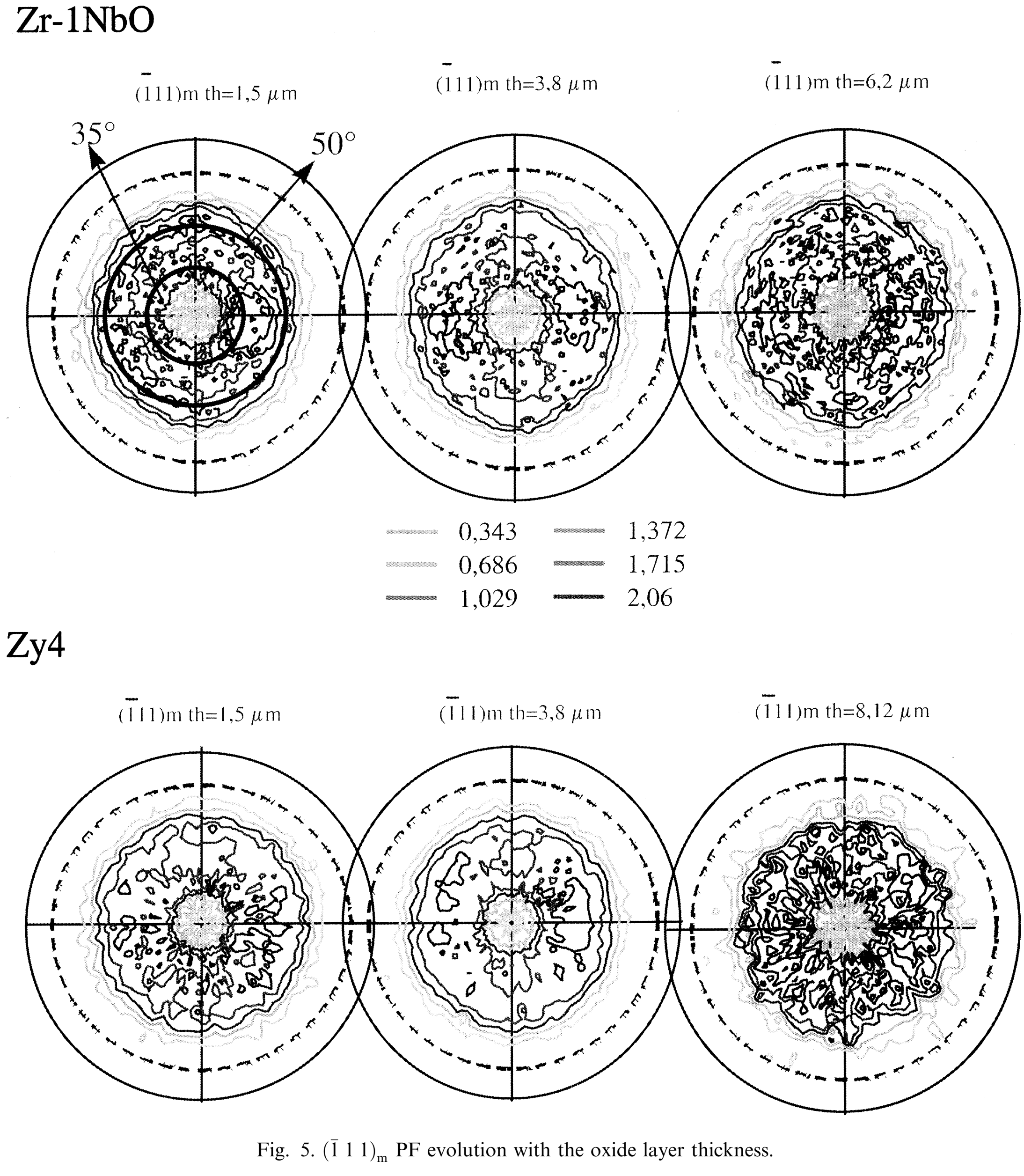

Fig. 5. $(\bar{1}\,1\,1)_m$ PF evolution with the oxide layer thickness.

Table 3
Texture factors for the diffracting planes of the two alloys and their evolution with the incidence angle θ_i

Alloy	Zr–1%NbO	Zy4
$n(\bar{1}\,1\,1)_m$	0.28	0.29
	0.43–0.015θ_i	0.39–0.013θ_i
$n(1\,1\,1)_t$	0.64	0.37
	1.54–0.061θ_i	0.7–0.032θ_i
$n(1\,1\,1)_m$	0.07	0.07

changing. A linear approximation is given in the same table. The former point makes clear that the tetragonal phase is also textured and suggests further investigation in this direction using advance techniques like synchrotron radiation [19].

3.2.2. In situ tetragonal zirconia fraction

The X-ray diffracted intensities are integral quantities linked to the phases analysed and their volume fractions in homogeneous and isotropic materials. The $(\bar{1}\,1\,1)_m$, $(1\,1\,1)_m$ and $(1\,1\,1)_t$ peaks have been acquired and recorded during the oxidation at 743 K. For crystallites growing with the same orientation, when the system is set in Bragg incidence, the $(h\,k\,l)$ reflecting plane intensities are described by the relation

$$I(h\,k\,l) = I_{\max}(h\,k\,l)\left(1 - e^{-\frac{2\mu h}{\sin\theta_{h\,k\,l}}}\right), \tag{12}$$

$I_{\max}$ being the maximum value recorded during an experiment. For the range of thickness studied, no $(\bar{1}\,1\,1)_m$ peak intensity drop was observed with any change in texture. For both alloys, the tetragonal fractions obtained have been plotted vs the oxidation times (Fig. 6). The tetragonal fraction is always higher for thin films and decreases continuously with oxide layer from 9% to 6% for Zr–1NbO and from 14% to 7% for Zy4, in the range studied. It should be noted that without texture correction, both alloys would have exhibited similar values, from 35–30% at the beginning of oxidation to 15–12% at the end of the experiment. Tetragonal content was found to be higher for Zy4 than for Zr–1NbO.

During the experiments, the samples have been cooled under vacuum to room temperature and the tetragonal content measured in situ at the end of each oxidation experiments. The same measurements were also performed at 743 K, just at the beginning of the next oxidation step. No evolution of tetragonal fraction has been detected, neither following this temperature cycle, nor during the measurement performed at room temperature. These results are in agreement with the earlier ones of David et al. [7]. Thus, ex situ tetragonal fraction measurements are in agreement with in situ measurements, and the evolution of phase fraction within the oxide thickness as well as gradients in the oxide layer can be studied after cooling.

3.2.3. Tetragonal phase gradients at room temperature

The tetragonal concentration gradient was determined by using the variable incidence method on samples of different oxide thickness. As the average diffracted intensities depend on the texture factor, this factor has been measured on each sample for each incidence thanks to the pole figures. Its evolution with the incident angle studied (θ_i between 3° and 14°) is weak but significant. The results are given in Table 3. A plot of the gradient computed for these samples is given in Fig. 7. Whatever the alloy, the tetragonal content is higher near the metal/oxide interface and decreases continuously up to the oxide free surface. The gradient is more pronounced on the Zy4 alloy than on the Zr–1NbO and the tetragonal content is higher in the oxide layer grown on Zy4. These results are in

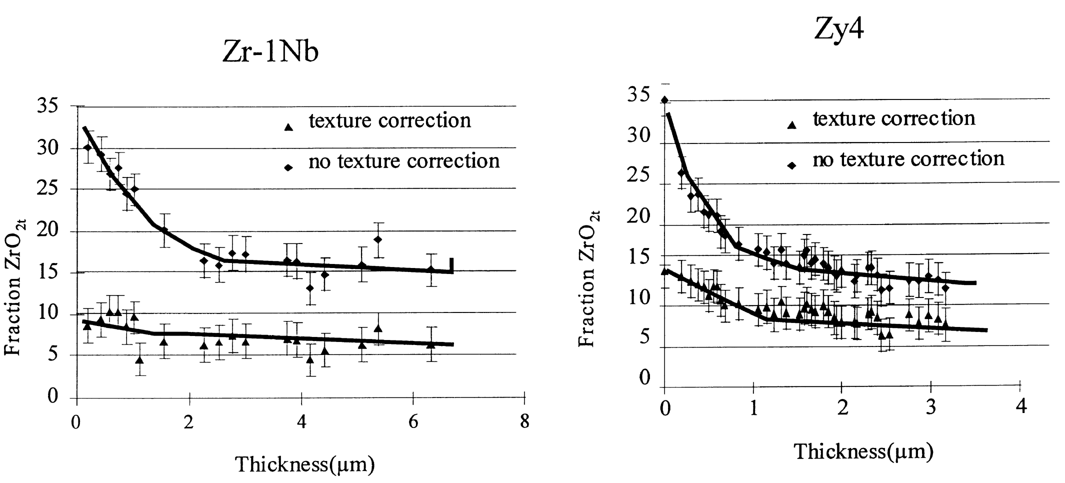

Fig. 6. Tetragonal proportion evolution in temperature with and without texture correction for each alloy.

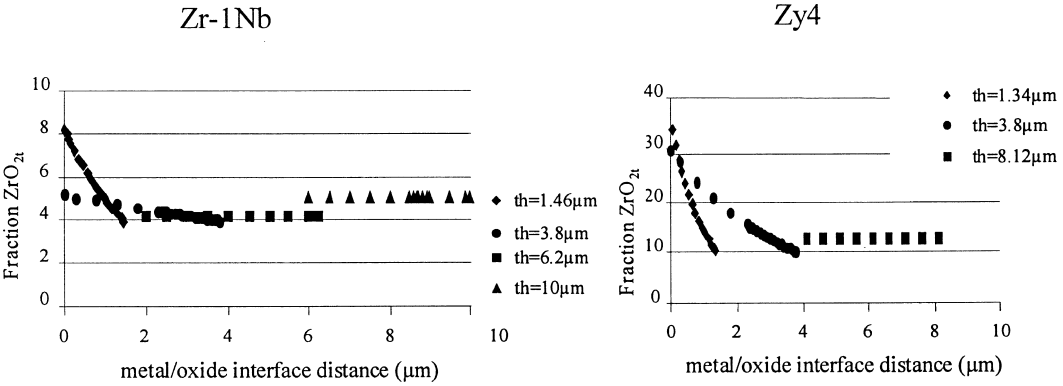

Fig. 7. Distribution of tetragonal fraction on samples of different thicknesses for the two alloys.

agreement with the average evolution at 743 K and after cooling. For the thicker samples (thickness greater than the penetration depth, whose typical value is 17 µm for 1/*e*), the tetragonal fraction appears to be constant in the outer part of the oxide layer (from which comes the diffracted intensity), but does not preclude any gradient near the metal/oxide interface.

3.3. Pseudo-stresses in the zirconia layer

When measured in situ at elevated temperature, pseudo-stresses in monoclinic zirconia (σ_{11}) are compressive for both alloys (Fig. 8). The stresses measured with the Zr–1NbO samples were high (-1.8 ± 0.3 GPa) and almost no change occurred with the oxidation time. However, for the Zy4 alloy, a stress relaxation occurred after approximately five days and then the stress level remained constant. In addition, the average magnitude is lower for Zy4 (between −200 and −500 MPa). No relaxation was detected in the case of Zr–1NbO, although the experiment was longer than for Zy4.

For the measurements of pseudo-stresses performed at room temperature on oxidized samples (Fig. 9), whatever the alloy, high compressive stresses develop in the oxide layer. For both alloys, pseudo-stresses seem to increase with the oxide thickness until a critical value was reached (about 1.8 µm for Zr–1NbO and 2.1 µm for Zy4). Afterwards, they decrease (more significantly for Zr–1NbO than for Zy4) and become steady, with similar values for both alloys (≈ -0.5–0.6 GPa). Compared to in situ measurements, the pseudo-stresses at room temperature are significantly different. These different values imply that in situ experiments must be performed and detailed analysis undertaken to get correct and, if possible, accurate stress values.

In order to precise this later point, at the end of the oxidation experiments, several cooling and heating

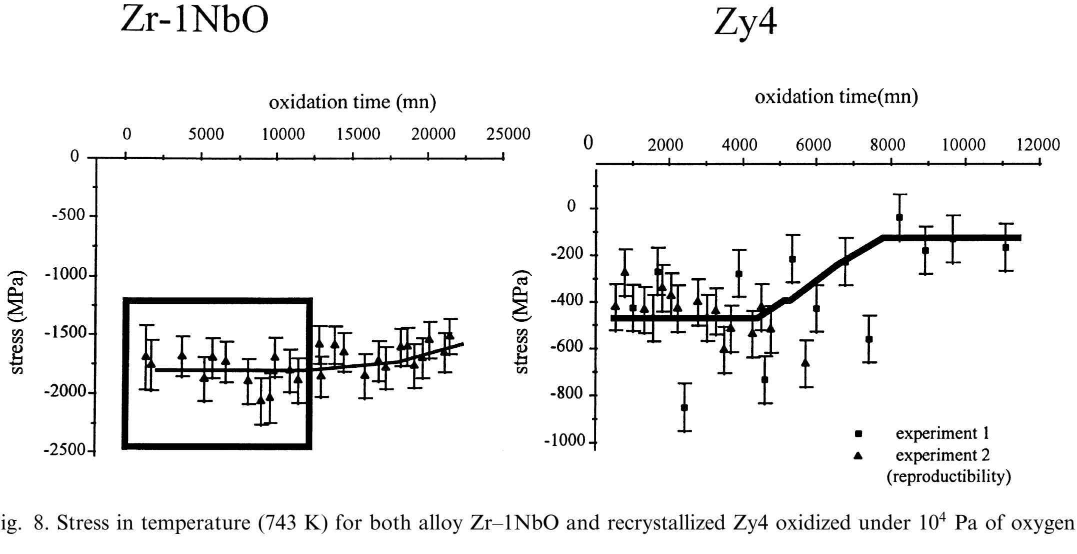

Fig. 8. Stress in temperature (743 K) for both alloy Zr–1NbO and recrystallized Zy4 oxidized under 10^4 Pa of oxygen.

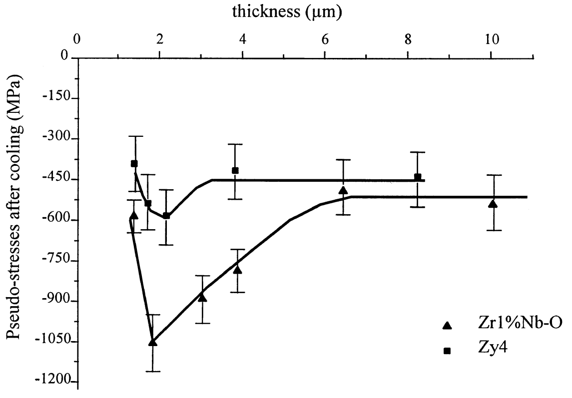

Fig. 9. Stress at room temperature (pseudo-stress) for both alloy Zr–1NbO and recrystallized Zy4 oxidized under 10^4 Pa of oxygen.

cycles have been performed on two samples oxidized for approximately 10 days. The XRD measurements at elevated temperature were performed under the oxidizing conditions to avoid dissolution of the oxide layer in the base metal. The measurements performed during these temperature cycles clearly show a very strong temperature dependency of the stress state in the monoclinic zirconia (Fig. 10). This dependency is very reproducible: along the thermal cycling, for a same temperature, the pseudo-stresses do not evolve significantly, taking into account the measurement accuracy. For Zr–1NbO, the stress state at room temperature is compressive of the order of −400 MPa, while at elevated temperature (743 K) the compressive stresses are increased to −1700 MPa. For Zy4, the effect is reversed, although the difference in stresses at the two temperatures is less important.

The differences found between the measurements performed at these two temperatures should be related to thermally induced stresses. Later, when these are calculated according to Huntz's model [22], taking into account macroscopic thermal expansion coefficient differences between ZrO_2 and the Zr alloys, thermal stresses can hardly exceed 100 MPa. This value is by far not high enough to explain the difference experimentally measured. Another approach has to be developed considering both the thermal expansion of each phase and the tetragonal contents in the oxide layer.

4. Discussion

The main items that could be discussed are related to the zirconium oxide film microstructure and behaviour, the relations between phases, stress changes during temperature cycling and oxidation kinetics, and some consequences of the difference in behaviour between the two alloys.

4.1. Thermal stresses during temperature changes

During the oxidation of Zr alloys in temperature, the high Pilling–Bedworth ratio for Zr/ZrO_2 leads to the buildup of compressive stresses in the oxide, since it grows at the metal/oxide interface. Several experiments have confirmed such high compressive stresses in the Zr oxide layers [14,23,24]. The experiments reported in this paper confirm such stress states and, in addition, give information on their variations with temperature. The slopes found in the $2\theta_{\phi\psi} = f(\sin^2\psi)$ adjustment lines are not the same at room temperature and at 743 K. For Zr–1NbO, the classical stress analysis by X-rays [16]

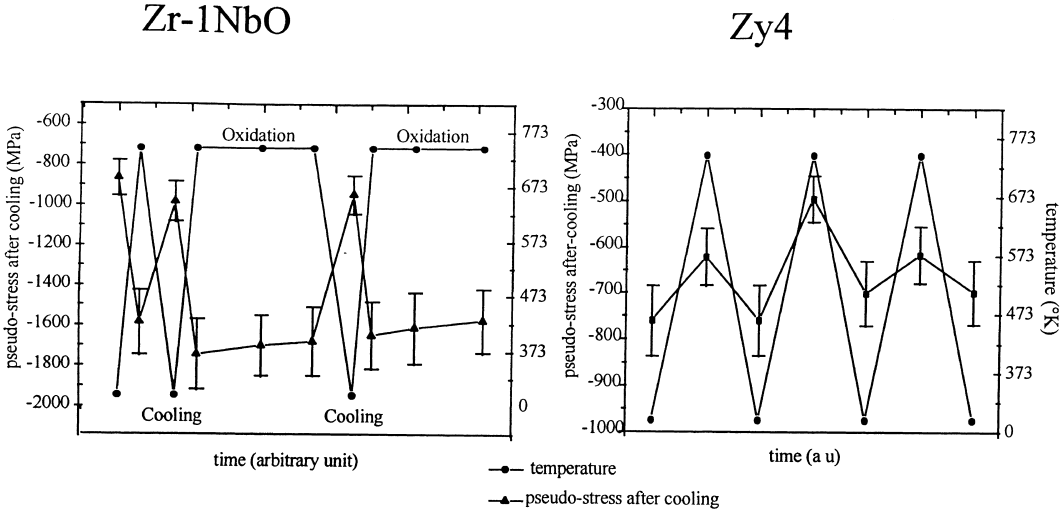

Fig. 10. Pseudo-stress after heat/cooling cycle for both alloy Zr–1NbO and recrystallized Zy4 oxidized under 10^4 Pa of oxygen.

performed on these data, using an average value of the elastic modulus of the monoclinic zirconia, leads to compressive stresses of about -1800 ± 150 MPa at 743 K, reducing to -850 ± 100 MPa at room temperature, similar to what has been reported in earlier experiments performed at room temperature [13,15,17]. However, the large differences observed between the two temperatures of data acquisition raise the question of the exact meaning and value of the 'stresses' during the oxidation process.

In the case of multiphase materials on a substrate, the exact transfer function linking strains measured on one phase by X-rays and the stress tensors is still not available [16]. However, an approximate analysis can be undertaken tentatively. The aim of this section is to give a preliminary analysis of the lattice parameters measured in order to have a better view of the stress-state during oxidation at 743 K and the changes induced by the cooling to room temperature.

The $2\theta_{\phi\psi} = f(\sin^2\psi)$ plots reported in Fig. 2 show two main behaviours for the two temperatures: the slopes are different but also the values of θ_0 a quantity related to the reference stress free lattice parameter. For the measurements of the thermal stresses, the shift in lattice parameter has to be referred to a given value of θ_0. Since this value is changing with temperature, a question arises on the physical meaning of this $\Delta\theta_0$. Two contributions could be suspected for this change: the free thermal expansion for ZrO_2 and the strain induced by the thermal expansion of the Zr alloy substrate. Both values are too small to explain the found $\Delta\theta_0$. Thermal strains are, thus, expected to develop on the $(\bar{1}\,0\,4)_m$ planes by thermal strain incompatibilities between the two zirconia phases.

In order to predict the contribution of such thermal strains, a detailed knowledge of the thermoelastic properties of the two phases of the zirconia is required.

For the monoclinic phase, the thermal expansion coefficients have been compiled by Touloukian et al. [25]. For the tetragonal zirconia, since this phase does not exist at room temperature for pure ZrO_2, the values were obtained by extrapolating the measurements performed on Y-TZP and on Ce-TZP [26,27] to zero addition content. The values obtained are given in Table 4. It should be pointed out that the thermal expansion of the zirconia is highly anisotropic and that very large differences are observed between the αs for the different phases and crystallographic directions.

The elastic coefficients have been measured on single crystals of monoclinic zirconia [28,29]. The corresponding Young's moduli in different directions are given in Table 4. The elastic anisotropy is very large, and a specific warning should be made on the minimum stiffness in the $[\bar{1}\,0\,4]$ direction corresponding to the lattice planes used for the XRD experiments. For the tetragonal phase, the only data set found is based on lattice parameter measurements by neutron diffraction of stressed Ce-TZP. Again a large anisotropy (a factor of 3) is clearly evidenced.

4.1.1. Thermal stresses in zirconia

For polycrystalline zirconia, due to the thermoelastic properties of each phase, any change in temperature induces internal stresses. Unfortunately the lattice plane chosen for reasons of simplicity in the stress measurements ($[\bar{1}\,0\,4]$), has a high thermal expansion coefficient and a low modulus of elasticity along its normal. In the case of an isotropic spatial distribution of the crystallite orientations (like bulk zirconia after powder sintering), the thermal stresses would be the same whatever the orientation of the planes analyzed. After cooling, certain planes, e.g., $[\bar{1}\,0\,4]$, will always be found in tension, balanced by others, with different $[h\,k\,l]$, e.g., [0 1 0], in compression, the weighted average being zero. In the extreme case where the relative orientation of the crystallite and its surrounding environment leads to the highest mismatch, the $(\bar{1}\,0\,4)$ planes would support a $\Delta\sigma$ of about 730 MPa for a $\Delta T = 450$ K. Had some tetragonal phase fraction been considered, higher values of $\Delta\sigma$ would have been obtained.

However, the zirconia growing during Zr alloy oxidation is highly textured, the $(\bar{1}\,0\,k)$ planes with high k are close to being parallel to the surface, with a very high intensity for the $(\bar{1}\,0\,4)$ and $(\bar{1}\,0\,3)$ planes. This corresponds to the direction [0 1 0] parallel to the surface. Thus, as Ψ is increased, the $(\bar{1}\,0\,4)$ planes analyzed are less numerous and more perpendicular to the surface. Then the crystals examined are changing their crystallographic environments, due to the crystallographic texture. Assuming for simplicity a fibre texture with $[\bar{1}\,0\,4]$ direction perpendicular to the surface, the thermal expansion of the zirconia layer decreases from the one of

Table 4
Thermal expansion coefficient and elastic moduli of zirconia phases[a]

		a : [1 0 0]	b : [0 1 0]	c : [0 0 1]	Specific direction
α (K^{-1})	Monoclinic	8×10^{-6}	1.2×10^{-6}	12.6×10^{-6}	$[\bar{1}\,0\,4]$: 12.4×10^{-6}
	Tetragonal	10.5×10^{-6}		15.2×10^{-6}	
E (GPa)	Monoclinic	290	282	180	$[\bar{1}\,0\,4]$: 145
	Tetragonal	360		273	[1 1 1] : 126

[a] α and E averaged over 300–700 K.

the $[\bar{1}\,0\,4]$ direction at $\Psi = 0(\alpha_{(\psi=0)} = \alpha_{[\bar{1}\,0\,4]})$ to a third of it at $\Psi = \pi/2$ (average value of the $[0\,1\,0]$ and $[1\,0\,0]$ directions).

Due to the texture of the zirconia, the $[\bar{1}\,0\,4]$ planes examined at low Ψ are only very few having the orientation corresponding to the selected diffraction conditions, and thus will have to follow the thermal strains imposed by the surrounding zirconia. This leads to the following thermal strains on the analyzed planes:

$$\begin{aligned}\varepsilon_{\Psi} &= \Delta T(\alpha_{(\Psi=0)}\cos^2\Psi + \alpha_{(\Psi=\pi/2)}\sin^2\Psi) \\ &= \Delta T[\alpha_{(\Psi=0)} + (\alpha_{(\Psi=\pi/2)} - \alpha_{(\Psi=0)})\sin^2\Psi], \qquad (13)\end{aligned}$$

a distribution similar to what would be expected from surface stresses using the standard analysis by continuum mechanics described in Section 2.2.3. The thermoelastic constants given in Table 4 lead to a contribution of the thermal stresses equivalent of the lattice strain measured at $\psi = 0$, and to 1/2 of the strain at $\sin^2\psi = 0.5$. This confirms that the $[\bar{1}\,0\,4]$ planes are stressed by a combination of swelling stresses due to the oxide growth and of thermal stresses induced by thermoelastic incompatibilities within the zirconia layer.

Thus, what is called 'stresses in the oxide' is a variable quantity, depending on the scale of analysis. Considered at the scale of the continuum mechanics it can be measured by macroscopic effects such as bending of the sample during one-sided oxidation. But at the oxide grain scale the stresses are dependent of grain orientations. A consequence of this is that measurements of stresses using a technique having a probe size working at that level (X-rays, Raman shift etc.) is biased by internal thermal stresses, unless performed in situ. Rough thermoelastic analysis of their magnitudes leads to the conclusion that they are of the same order of magnitude as the oxide swelling stresses. Clearly, the analysis has to be developed in more detail, using homogenization techniques for thermoelastic strain computations, including real texture data instead of the fibrous approximation. This would have been out of the scope of the paper. However, such an approach is underway and will allow to bring together the various phenomena involved in thermoelastic behaviour of the zirconia layer (ZrO_2 microstructure, oxide layer thickness, two phases for zirconia, textures of the phases, grain shapes, Zr alloy substrate etc.).

4.2. Stress state, type of phases and oxidation kinetics

As discussed above, the stresses measured on the $[\bar{1}\,0\,4]$ planes of the monoclinic zirconia are not direct measurements of the average stress tensor components in the oxide layer. However, the quantities measured, referred as 'pseudo-stresses' could be used qualitatively to analyse the effects of stress state on phase fraction.

Concerning the relation between the stresses and the tetragonal content, it is clear by comparing the two alloys that the stresses are not the main factor acting on the tetragonal stabilization: the highest pseudo-stresses are obtained on Zr–1NbO, where the tetragonal content is the lowest. In addition, as discussed previously, a significant drop of tetragonal fraction was obtained, both with oxidation time and with the oxide thickness, while the pseudo-stresses did not modify significantly.

With respect to the tetragonal phase content, the measurements confirm that the tetragonal phase is not evenly distributed, and that higher levels exist near the metal/oxide interface. Such gradients have been already evidenced and several explanations of these gradients have been proposed [13,30,31]. On both alloys, the average tetragonal content decreases continuously and smoothly, independent of the kinetic transitions of the alloys, as the oxidation proceeded. It means that there is no sharp or sudden evolution throughout the bulk of the oxide layer. However, it does not preclude to a local sharp decrease at the metal/oxide interface for thick oxide layers. In other conditions of oxidation (high pressure steam), similar results have been obtained on Zy4 type alloys [31]. Also for various Zr–Nb alloys, different evolutions can be found in the literature, such as an increase followed by a decrease of the tetragonal fraction on Zr–2.5Nb alloys [1].

Having in mind the fact that the kinetic curves (weight gain) are related to the whole oxide thickness, while the phase fractions and pseudo-stress measurements concern mainly the outer part of the film due to absorption coefficient of zirconia, it appears that the texture of the oxide film is roughly constant, whatever the alloy and the oxidation time. This observation is consistent with other studies. It has been proposed [17] that such a texture develops in order to minimize the stored elastic energy in the oxide layer, taking into account the anisotropy in elastic constants of the monoclinic zirconia.

With respect to the impact of stresses on corrosion kinetics, a few comments could be made: The experimental results presented suggest that there is no evolution of 'pseudo-stresses' within the thickness of the oxide layer, at least at the beginning of oxidation. As the X-ray probe size (penetration depth) is small for pseudo-stresses measurements (due to the high diffraction angle and the large wavelength), it is likely that there is no or only a small gradient at the beginning. This could be in disagreement with some results obtained by Godlewski using Raman spectroscopy on the monoclinic peaks on taper sections of the oxide layers [24]. The differences could be related to specific measurement conditions: the present study is concerned only with the pseudo-stresses in the plane of the oxide/metal interface, and they are determined in situ. In the experiments using Raman spectroscopy, the stress directions cannot be defined. In addition, they have been performed at room temperature and no consideration for the thermal stresses induced by cooling from autoclave testing temperature has been made for the analysis of the corrosion at elevated temperature.

If pseudo-stresses are supposed to be homogeneous throughout the oxide thickness at the beginning of the oxidation, no drop at the surface is seen when the oxide grows up to the kinetics transition. Therefore, the transition does not seem associated with a sudden stress release, but rather as observed on TEM [11], by the creation of cracks in the oxide, which act first as a barrier to oxidizing species, and then, when connected to the outer surface, as new external boundary.

4.3. Comparison of Zy4 and Zr–1NbO

A major difference between Zy4 and Zr–1NbO oxidation behaviour is the very weak transition of the latter. This difference of corrosion kinetics between the two alloys has been proposed to be explained by different controlling steps of the oxidation mechanism for Zy4 and Zr–1NbO (diffusion of oxygen vs surface reaction kinetics) [11]. The influence of the oxygen pressure is another argument of this difference in controlling mechanisms. The Zr–1NbO alloy, compared to recrystallised Zy4, shows in the conditions analysed a higher oxidation kinetic, a lower tetragonal content and higher pseudo-stresses. It is worth noting that the testing conditions (743 K and 10 kPa O_2) chosen for this analytical work are far from those encountered in PWRs during irradiation (600 K, H_2O and $[O] < 20$ ppb) [32].

The lower tetragonal content of the Zr–1NbO is expected to improve the corrosion resistance under water environment as this phase transforms into the monoclinic one as the oxidation proceeds. Indeed this transformation is partly responsible for the development of the porosity in the oxide layer.

Solid solution components could have an effect on the structure of the zirconia. For instance the valence state in the zirconia of the addition elements in solid solution in the metal is expected to be different: Sn is presumably not oxidized at the metal/oxide interface while Nb should be. This would affect the charged point defect density and, thus, the stability of the different phases of the zirconia. It is also likely that the higher grain size and lowest oxygen vacancy concentration at the metal/oxide interface in Zr–1%Nb favours the monoclinic phase in spite of the tetragonal.

In addition, the other structural parameters of the alloys are known to have a high impact on the oxidation behaviour. For instance, the effect of the intermetallics in Zy4 or of the β-Nb precipitates in Zr–1NbO were not considered in this work. The role of these second phase particles is still a matter of discussion although it is known to be of high importance.

5. Conclusions

Two zirconium alloys have been oxidized at low oxygen pressure and high temperature, and followed in situ and after cooling for the stresses and phase content by XRD. The following points have been shown: (1) No obvious relation between phases of the zirconia, stresses and kinetic transition appears, the tetragonal phase being therefore not mainly stabilized by compressive stresses. (2) Zr–1NbO alloy presents, under these particular conditions (fairly different from the PWR ones), a higher oxidation kinetic than recrystallised Zy4, together with a lower tetragonal content and higher pseudo-stresses. (3) Upon cooling, no significant change in tetragonal content occurs, and the stress changes measured on $[\bar{1}\,0\,4]$ monoclinic zirconia during temperature changes are totally reversible. A large contribution of thermoelastic stresses is thus expected to be included in the quantities measured.

A first-order analysis of these results, based on the highly anisotropic thermoelastic behaviour of the zirconia, and on its textured growth, allows one to highlight the importance of thermoelastic stresses arising during cooling of samples after oxidation, the magnitude of which being similar to the phenomena aimed to be measured.

As a consequence, to obtain reliable values of the oxide stresses it is necessary to analyze the results of such measurements with a procedure including considerations for accurate knowledge of the thermoelastic properties of the phases, the microstructure (grain sizes and shapes, textures) and the thermal history of the sample.

Acknowledgements

We thank Cézus and Burgundy region for their financial support in this work. We gratefully acknowledge Dr F. Lefebvre-Joud (CEA, Grenoble, France), for helpful discussions and all her remarks on this work.

References

[1] A.J.G. Maroto et al., J. Nucl. Mater. 229 (1996) 79.
[2] B. Cox, Adv. in Corrosion Sci. and Tech., Plenum, New York, 1976, p. 173.
[3] B. Cox, V.G. Kritsky, C. Lemaignan et al., Waterside corrosion of zirconium alloys in nuclear power plants, TecDoc 996, IAEA, 1998.
[4] J. Adams, B. Cox, J. Nucl. Energy A 11 (1959) 31.
[5] G. Wilmark et al., ASTM-STP 1295 (1995) 55.
[6] F. Garzarolli et al., ASTM-STP 1132 (1991) 395.

[7] G. David, R. Geschier, C. Roy, J. Nucl. Mater. 38 (1971) 329.
[8] H.P. Klug, L.E. Alexander, X-ray Diffraction Procedures, Wiley, New York, 1954.
[9] R.C. Garvie, P.S. Nicholson, J. Am. Ceram. Soc. 55 (1972) 303.
[10] Ch. Valot, D. Ciosmak, M.T. Mesnier, M. Lallemant, Oxid. Met. 48 (1997) 329.
[11] P. Bossis, G. Lelièvre, P. Barberis, X. Iltis, F. Lefebvre, ASTM-STP 1354 (2000) 918.
[12] X. Iltis, F. Lefebvre, C. Lemaignan, J. Nucl. Mater. 224 (1995) 109.
[13] J. Godlewski et al., ASTM-STP 1132 (1991) 416.
[14] F. Garzarolli, H. Seidel, R. Tricot, J.P. Gros, ASTM-STP 1132 (1991) 395.
[15] J.L. Bechade et al., High Temp. Mater. Process. 2 (1998) 359.
[16] O.V. Hauk, Adv. X-ray Anal. 39 (1997) 181.
[17] M. Parise, O. Sicardy, G. Cailletaud, J. Nucl. Mater. 256 (1998) 35.
[18] Y.P. Lin, O.T. Woo, D.J. Lockwood, Mater. Res. Soc. Symp. Proc. 343 (1994) 487.
[19] J.L. Béchade et al., in: Proc. ICRS-5, Linköping, Sweden, 16–18 June 1997.
[20] E. Kröner, J. Mech. Phys. Solids 15 (1967) 319.
[21] A. Reuss, Z. Angew, Math. Mech. 9 (1929) 49.
[22] A.M. Huntz, Mater. Sci. Technol. 4 (1988) 1079.
[23] C. Roy, B. Burgess, Oxid. Met. 2 (1970) 235.
[24] J. Godlewski, P. Bouvier, G. Lucazeau, L. Fayette, ASTM-STP 1354 (2000) 877.
[25] Y.S. Touloukian et al., Thermophysical Properties of Matter: Thermal Expansion, vol. 13, Plenum, New York, 1975, p. 451.
[26] T.S. Sheu, J. Am. Ceram. Soc. 76 (1993) 1772.
[27] P. Scardi, R. Di Maggio, L. Lutterotti, J. Am. Ceram. Soc. 75 (1992) 2828.
[28] M.V. Nevitt et al., Physica B 150 (1988) 230.
[29] S. Chan et al., J. Am. Ceram. Soc. 74 (1991) 1742.
[30] M. Parise, O. Sicardy, G. Cailletaud, J. Nucl. Mater. 256 (1998) 35.
[31] P. Barberis, J. Nucl. Mater. 226 (1995) 34.
[32] J.P. Mardon, D. Charquet, J. Senevat, ASTM-STP 1354 (2000) 505.